PASJ: Publ. Astron. Soc. Japan **60**, 919–931, 2008 August 25

Multiple-Component Analysis of the Time-Resolved Spectra of GRB 041006: A Clue to the Nature of the Underlying Soft Component of GRBs

Yuji SHIRASAKI,[1] Atsumasa YOSHIDA,[2,4] Nobuyuki KAWAI,[3,4] Toru TAMAGAWA,[4] Takanori SAKAMOTO,[5] Motoko SUZUKI,[6] Yujin NAKAGAWA,[2] Akina KOBAYASHI,[2] Satoshi SUGITA,[2,4] Ichiro TAKAHASHI,[2] Makoto ARIMOTO,[3] Takashi SHIMOKAWABE,[3] Nicolas Vasquez PAZMINO,[3] Takuto ISHIMURA,[3] Rie SATO,[7] Masaru MATSUOKA, [6] Edward E. FENIMORE, [8] Mark GALASSI, [8] Donald Q. LAMB, [9] Carlo GRAZIANI, [9] Timothy Q. DONAGHY, [9] Jean-Luc ATTEIA, [10] Alexandre PELANGEON, [10] Roland VANDERSPEK, [11] Geoffrey B. CREW, [11] John P. DOTY, [11] Joel VILLASENOR, [11] Gregory PRIGOZHIN, [11] Nat BUTLER, [11,12] George R. RICKER, [11] Kevin HURLEY, [12] Stanford E. WOOSLEY, [13] and Graziella PIZZICHINI [14]

[1] *National Astronomical Observatory of Japan, 2-21-1 Osawa, Mitaka, Tokyo 181-8588*
yuji.shirasaki@nao.ac.jp
[2] *Department of Physics and Mathematics, Aoyama Gakuin University, 5-10-1 Fuchinobe, Sagamihara, Kanagawa 229-8558*
[3] *Department of Physics, Tokyo Institute of Technology, 2-12-1 Ookayama, Meguro-ku, Tokyo 152-8551*
[4] *RIKEN, 2-1 Hirosawa, Wako Saitama 351-0198*
[5] *Goddard Space Flight Center, NASA, Greenbelt, MA 20771, USA*
[6] *JAXA, 2-1-1 Sengen, Tsukuba, Ibaraki, 305-8505*
[7] *JAXA/ISAS, 3-1-1 Yoshinodai, Sagamihara, Kanagawa 229-8510*
[8] *Los Alamos National Laboratory, P.O. Box 1663, Los Alamos, NM 87545, USA*
[9] *Department of Astronomy and Astrophysics, University of Chicago, 5640 South Ellis Avenue, Chicago, IL 60637, USA*
[10] *LATT, Université de Toulouse, CNRS, 14 avenue E. Belin, 31400 Toulouse, France*
[11] *Center for Space Research, MIT, 77 Vassar Street, Cambridge, Massachusetts, 02139-4307, USA*
[12] *Space Sciences Laboratory, 7 Gauss Way, University of California , Berkeley, California, 94720-7450*
[13] *Department of Astronomy and Astrophysics, University of California at Santa Cruz, 477 Clark Kerr Hall, Santa Cruz, CA 95064, USA*
[14] *INAF/IASF Bologna, Via Gobetti 101, 40129 Bologna, Italy*

(Received 2008 February 12; accepted 2008 April 14)

Abstract

GRB 041006 was detected by HETE-2 on 2004 October 06. The light curves in four different energy bands display different features. At higher energy bands several peaks are seen in the light curve, while at lower energy bands a single broader bump dominates. It is expected that these different features are the result of a mixture of several components, each of which has different energetics and variability. We analyzed the time-resolved spectra, which were resolved into several components. These components can be classified into two distinct classes. One is a component that has an exponential decay of E_p with a characteristic timescale shorter than $\sim 30\,\mathrm{s}$; its spectrum is well represented by a broken power-law function, which is frequently observed in many prompt GRB emissions, so it should have an internal-shock origin. Another is a component whose E_p is almost unchanged with a characteristic timescale longer than $\sim 60\,\mathrm{s}$, and shows a very soft emission and slower variability. The spectrum is characterized by either a broken power law or a black-body spectrum. By assuming that the soft component is a thermal emission, the radiation radius is initially $4.4 \times 10^6\,\mathrm{km}$, which is a typical radius of a blue supergiant, and its expansion velocity is $2.4 \times 10^5\,\mathrm{km\,s^{-1}}$ in the source frame.

Key words: gamma-rays: bursts — X-rays: bursts — X-rays: individual (GRB 041006)

1. Introduction

On 2004 October 6, the High Energy Transient Explorer 2 (HETE-2) detected a gamma-ray burst (GRB) with soft X-ray emission before onset of the main event. Such soft emission, a precursor, is predicted in some of theoretical models. The fireball undergoes a transition from an optically thick phase to an optically thin phase, and thermal radiation (the fireball precursor) may occur during this transition (Paczyński 1986; Daigne & Mochkovitch 2002). A precursor (progenitor precursor) may also be emitted by the interaction of the jet with the progenitor star (Ramirez-Ruiz et al. 2002; Waxman & Meszaros 2003). The external shock by the first relativistic shell can also produce a non-thermal precursor (Umeda et al. 2005).

Soft precursors are occasionally detected in long GRBs. The first detection was made by the GINGA satellite (GRB 900126; Murakami et al. 1991). In more recent observations, the BeppoSAX (e.g., GRB 011121: Piro et al. 2005), HETE 2 (e.g., GRB 030329: Vanderspek et al. 2004), and Swift (e.g., GRB 050820A: Cenko et al. 2006; GRB 060124: Romano et al. 2006; GRB 061121: Page et al. 2007) satellites have also detected precursors. Lazzati (2005) studied bright long BATSE GRB light curves, and found that in 20% of the cases there is evidence for soft emission before the main event.

The precursor is usually detected as a single pulse that is well separated in time from the main event, typically several seconds to hundreds of seconds. The precursor of GRB 041006 is not well separated from the main event, and is likely to be continuously active during the whole prompt GRB phase. Such a long-lasting soft component was also observed in GRB 030329 (Vanderspek et al. 2004). Vetere et al. (2006) found that for some of the GRBs detected by the BeppoSAX, there is a slowly varying soft component underlying the highly variable main event. Borgonovo et al. (2007) analyzed the light curves obtained by BATSE, Konus, and BeppoSAX, and found that the width of the auto-correlation function shows a remarkable bimodal distribution in the rest-frame of the source. This result suggests that there exists a slowly varying soft component in some GRBs. The relation between the underlying soft X-ray component, the X-ray precursor, and the main event is still open to question.

In this paper, we present the results of multiple component analysis of the time-resolved spectra of GRB 041006. Throughout this paper the peak energies are in the observer's frame, and quoted errors are at the 90% C.L., unless specified otherwise.

2. Observation

GRB 041006 was detected with the HETE FREGATE (Atteia et al. 2003) and the WXM (Shirasaki et al. 2003) instruments at 12:18:08 UT on 2004 October 06 (Galassi et al. 2004). The WXM flight software localized the burst in real time, resulting in a GCN Notice 42 s after the burst trigger. The prompt error region was a circle of 14′ radius (90% confidence) centered at $00^{\mathrm{h}}54^{\mathrm{m}}54^{\mathrm{s}}$, $+01^\circ 18' 37''$ (J2000.0). A ground analysis of the burst data allowed the error region to be refined to a circle of 5.′0 radius (90% confidence) centered at $00^{\mathrm{h}}54^{\mathrm{m}}53^{\mathrm{s}}$, $+01^\circ 12' 04''$ (J2000.0).

Then, 1.4 hours after the trigger, the optical afterglow was found by Da Costa et al. (2004), and the redshift was first reported by Fugazza et al. (2004) and later confirmed by Price et al. (2004) to be $z = 0.716$. Follow-up observations were made at various observation sites (e.g., Urata et al. 2007). VLA observations were made, but no radio sources were detected (Soderberg et al. 2004). The X-ray afterglow was found by Butler et al. (2005), and it exhibited a power-law decay with a slope of -1.0 ± 0.1. The X-ray spectrum was characterized by an absorbed power-law model with a photon index of $\Gamma = 1.9 \pm 0.2$ and $n_{\mathrm{H}} = (1.1 \pm 0.5) \times 10^{21}\,\mathrm{cm}^{-2}$. The emergence of a supernova component was reported by Bikmaev et al. (2004) and Garg et al. (2004). The field of GRB 041006 was imaged by Soderberg et al. (2006) using the WFC of the ACS on-board HST; they found a SN 1998bw-like supernova dimmed by ~ 0.3 magnitudes.

3. Analysis

The data obtained by the WXM and FREGATE instruments were reduced and calibrated in the standard manner. We used WXM TAG data and FREGATE PH data.

3.1. Temporal Properties

Figure 1 shows the light curves of GRB 041006 in four energy bands with a 0.5 s time resolution. T_{50} and T_{90} were measured for each energy band, and are shown in table 1.

The burst can be divided into four major intervals according to the spectral features, and each major interval is divided into a few sub-intervals for time-resolved spectral analysis. The time intervals for each sub-interval are given in table 2. In interval 1, soft emission showing no prominent activity above 40 keV occurred, then harder emissions followed in intervals 2 and 3. In interval 4, the hard emission almost disappeared and only gradually decaying soft emission was present.

We call the emission seen in interval 1 an X-ray precursor. The precursor shows a structured light curve in the lowest energy band (2–10 keV), which indicates that two emissions were occurring successively. In interval 2, two peaks were seen in the higher energy bands (> 40 keV). The time history of the hardness ratio also clearly shows the corresponding peaks. In the lowest energy bands (< 10 keV), structured emission was not clearly seen. In interval 3, two harder peaks were seen in the highest energy band (80–400 keV), and this structure was less distinct in the lower energy bands. The emission in interval 4, which we call an X-ray tail, showed no prominent structure.

From the dissimilarity of the light curves in the four energy bands, it is inferred that the total emission was composed of several independent emissions that had different characteristic energies. For example, two components that contributed to the precursor, four components were seen as a peak in the energy bands 40–80 keV and 80–400 keV, and one broad soft component constituting the major part of the light curve in the lowest energy band. To investigate this hypothesis, we performed a time-resolved spectral analysis based on a multiple-component spectrum model.

3.2. Average Spectral Properties

The joint spectral analysis of WXM and FREGATE data was performed using XSPEC v.11.3.1 (Arnaud 1996). The time-integrated spectrum of GRB 041006 is approximately described by a broken power law function (figure 2); the low-energy photon index is $\alpha = 1.28 \pm 0.02$, the high-energy index is $\beta = 2.14 \pm 0.07$, the break energy is $E_{\mathrm{p}} = 22.5 \pm 1.7$ keV and the flux at 1 keV is $K = 4.25 \pm 0.15\,\mathrm{cm}^{-2}\mathrm{s}^{-1}\mathrm{keV}^{-1}$, where the quoted errors are one sigma. The χ^2 is 111.19 for 79 dof, and the null hypothesis probability is 0.0099, so the fit is not very good. From this fitting result, we obtained $S_{\mathrm{X}} = (5.24 \pm 0.08) \times 10^{-6}\,\mathrm{erg\,cm}^{-2}$, $S_\gamma = (7.13 \pm 0.12) \times 10^{-6}\,\mathrm{erg\,cm}^{-2}$, where S_{X} and S_γ denote the fluences in the 2–30 keV and 30–400 keV energy ranges, and the error is 1 sigma. Since the ratio of the fluences is $\log(S_{\mathrm{x}}/S_\gamma) = -0.13$, GRB can be classified as an X-ray rich GRB (Sakamoto et al. 2005).

The isotropic energy is calculated from:

$$E_{\mathrm{iso}} = \frac{4\pi D_{\mathrm{L}}^2}{z+1} \int_{E_{\mathrm{lo,src}}/(z+1)}^{E_{\mathrm{hi,src}}/(z+1)} E\Phi dE \quad (1)$$

where D_{L} is the luminosity distance, Φ is the differential photon spectrum, and the range of energy integration is from

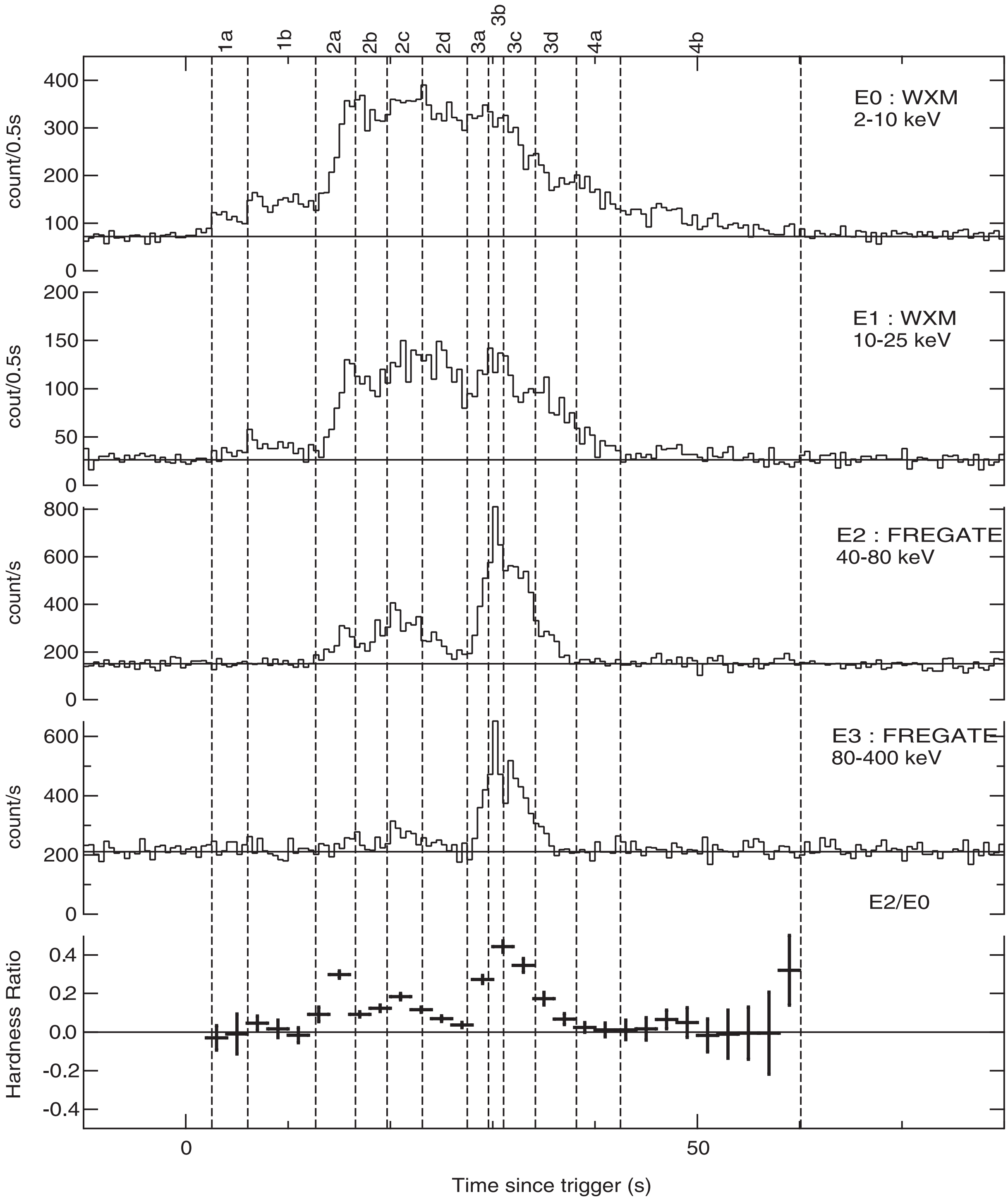

Fig. 1. Light curves of GRB 041006 in four energy bands and the hardness ratio. From top to bottom: 2–10 keV, 10–25 keV, 40–80 keV, and 80–400 keV. The hardness ratio was calculated by dividing the 40–80 keV count rate by the 2–10 keV count rate. The vertical lines represent the boundaries of the time intervals for a time-resolved spectral analysis.

1 keV to 10000 keV in the source frame. We obtained $E_{\rm iso}$ $= 2.54^{+0.46}_{-0.35}\times\ 10^{52}$ erg. In figure 3, the peak energy in the source frame $E_{\rm p,src}$ is plotted against the isotropic energy, $E_{\rm iso}$ (the point labeled "Total"). The relation for GRB 041006 obtained from the one component fit is completely outside the Amati relation (Amati 2006).

Looking at the residual plot in the left panel of figure 2, an additional soft component is apparently seen around 6 keV and a systematic excess is also seen around 50–100 keV. Thus, the total spectrum was fitted by a superposition of multiple basic functions. As basic functions, we considered a broken power law and a black body.

Table 1. Temporal properties, T_{50} and T_{90}, of GRB 041006.

Energy range (keV)	$T50^*$ (s)	$T90^*$ (s)
2–10	13.9 ± 0.08	38.2 ± 0.40
10–25	11.9 ± 0.16	27.3 ± 1.44
40–80	10.2 ± 0.09	19.6 ± 0.10
80–400	3.7 ± 0.25	17.4 ± 0.25

* $T50$ ($T90$) is the duration of the time interval during which 50% (90%) of the total observed photons are detected. The start of $T50$ ($T90$) is defined by the time at which 25% (5%) of the total photons have been detected. The quoted errors correspond to one sigma.

Table 2. Time intervals used for time-resolved spectral analysis.

Time interval	Start*–End* (s)
1a	2.5– 6.0
1b	6.0–12.5
2a	12.5–16.5
2b	16.5–19.5
2c	19.5–23.0
2d	23.0–27.5
3a	27.5–29.5
3b	29.5–31.0
3c	31.0–34.0
3d	34.0–38.0
4a	38.0–42.5
4b	42.5–60.0
2a’	15.0–16.5
2c’	22.0–24.0
3b’	30.0–32.0
3c’	33.0–35.0

* The offset time is the trigger time 2004-10-06 12:18:08.63933.

For the broken power-law model, we used the following function to estimate the peak energy flux directly:

$$A(E) = K/E_{\mathrm{p}}^2 (E/E_{\mathrm{p}})^{-\alpha}, \qquad E \leq E_{\mathrm{p}} \tag{2}$$
$$= K/E_{\mathrm{p}}^2 (E/E_{\mathrm{p}})^{-\beta}, \qquad E > E_{\mathrm{p}}.$$

The parameters α and β, which are the lower and higher energy photon indices, are restricted to the range of -2.0–2.0 and 2.5–5.0, respectively. The initial value of the break energy, E_{p}, of the `bknp` basic function was determined from the local excess of the residual between the single `bknp` model and the observed data. The restriction to the break energy, E_{p}, was applied so that the parameter would converge around the initial value.

The results of the spectral fit for three three-component models are given in table 3. For a comparison the results of the two-component model and a fit by the Band function (Band et al. 1993) and a broken power law function are also given in the table. The fitting parameters for the models `bbody*2+bknp` and `bknp*3` are given in table 4.

Akaike’s Information Criterion (*AIC*) was calculated for each model. *AIC* (Akaike 1974) is a very widely used criterion to evaluate the goodness of the statistical model from both the goodness of the fit and the complexity of the model. *AIC* is defined by the following equation:

$$AIC = n \ln\left(\frac{\chi^2}{n}\right) + 2k, \tag{3}$$

where n is the number of data points, k is the number of free parameters to be estimated, and χ^2 is the residual sum of squares from the estimated model. The *AIC* includes a penalty, which is an increasing function of the number of estimated parameters; overfitting is discouraged, and thus this method enables one to find the best model for the data, with the minimum of free parameters. The model with the lower value of *AIC* is the one to be preferred.

The most preferable model is `bbody*2+bknp`. The model name is given by an algebraic expression of the name of a basic

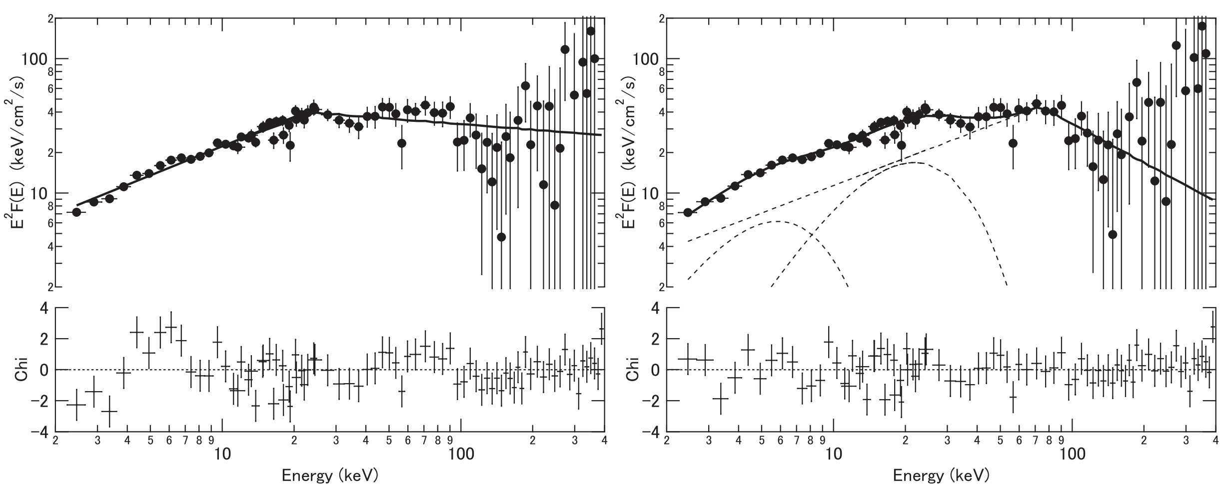

Fig. 2. Time-averaged unfolded spectrum expressed in νf_ν. Left: Fitting result for the broken power-law model. Right: Fitting result for the three-component model represented by a superposition of one broken power-law function and two blackbody functions.

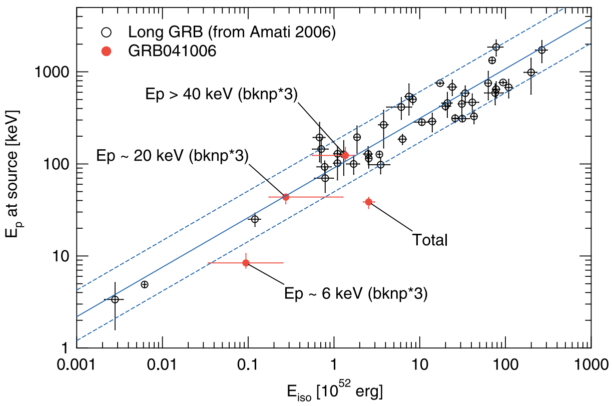

Fig. 3. $E_{\mathrm{p,src}}$–E_{iso} relation for long GRBs. The open circles represent the long GRBs compiled by Amati (2006). The solid circles represent GRB 041006. The solid circle labeled "Total" was derived from a single broken power-law model. The other solid circles were derived from a `bknp*3` model. The parameters obtained in this work are summarized in table 5. The solid line represents the average relation derived from all the points of the open circles, while the dashed lines represent lower and upper boundaries, which are parallel to the average relation and contain 90% of the points.

model. The second-most preferable model is `bknp*3`. The *AIC* values for the two models are 6.87 and 8.47 respectively.

The lowest *AIC* does not necessarily select the true model, and the degree of the preference is estimated by the *AIC* difference. The relation between the degree of the preference and the *AIC* difference (Δ_{X}), however, depends on n and the models to be compared. We thus evaluated the confidence limit of the *AIC* difference by carrying out a Monte Carlo simulation. The Monte Carlo simulation was performed by using the `fakeit` command of XSPEC, which generated 1000 PHA samples based on the spectral model to be tested. For each PHA sample, a spectral fit was performed for both the tested model and the model that gave the lowest *AIC*, and the *AIC* difference was calculated.

The left panel of figure 4 shows a simulated distribution of the *AIC* difference $\Delta_{\texttt{bknp*3}} = AIC_{\texttt{bknp*3}} - AIC_{\texttt{bbody*2+bknp}}$. The simulation was performed with the model spectrum `bknp*3`; the model parameters were obtained from the fit to the observed total spectrum. For each simulated PHA sample, a model fit was performed for both the `bknp*3` model and `bbody*2+bknp`, which is the most preferred model. From this result, the 90% confidence limit for $\Delta_{\texttt{bknp*3}}$ is estimated to be 4.7, below which 90% of the samples are included. Since the observed *AIC* difference for the model `bknp*3` is 2.64, the model is acceptable at the 90%

Table 3. Results of a spectral fit to the time-averaged spectrum.

Model	n^*	$k^\dagger$	$\chi^{2\ddagger}$	$p^\S$	$AIC^\Vert$	$\Delta_{\mathrm{X}}{}^\#$	Parameters**
bbody*2+bknp	83	8	74.35	0.499	6.87	—	$T = 1.4{,}5.5$, $E_{\mathrm{p}} = 74$
bknp*3	83	12	68.84	0.551	8.47	1.6 (4.7)	$E_{\mathrm{p}} = 5{,}25{,}72$
bbody+bknp*2	83	10	73.75	0.453	10.19	3.32 (4.1)	$T = 1.6$, $E_{\mathrm{p}} = 23{,}73$
bknp*2	83	8	77.80	0.390	10.63	3.76 (< 0)	$E_{\mathrm{p}} = 5{,}24$
band	83	4	96.55	0.087	20.55	13.68 (< 0)	$E_{\mathrm{p}} = 38$
bknp	83	4	111.19	0.010	32.27	25.40 (< 0)	$E_{\mathrm{p}} = 22$

* Number of data points used for the fit.
† Number of model parameters.
‡ Chi-square of the fit.
§ Null hypothesis probability.
‖ Akaike information criterion.
\# *AIC* difference between the corresponding model and the lowest *AIC* model. The numbers in parentheses represent the 90% confidence limits of the *AIC* difference.
** T is the black body temperature in keV and E_{p} is the break energy of the `brknp` model in keV.

Table 4. Fitting parameters for the time-averaged spectrum.

Model	Component	Parameters*			
bbody*2+bknp	1	$T = 1.40^{+0.22}_{-0.16}$	$K_{\mathrm{bbody}} = 0.16 \pm 0.04$		
	2	$T = 5.53^{+0.77}_{-0.67}$	$K_{\mathrm{bbody}} = 0.44 \pm 0.10$		
	3	$E_{\mathrm{p}} = 73.5^{+7.6}_{-15.6}$	$\alpha = 1.33^{+0.09}_{-0.14}$	$\beta = 2.96^{+1.19}_{-0.60}$	$K_{\mathrm{bknp}} = 37.8^{+6.2}_{-6.1}$
bknp*3	1	$E_{\mathrm{p}} = 71.9^{+16}_{-9.6}$	$\alpha = 1.3^{+0.2}_{-3.3}$	$\beta = 2.9^{+1.2}_{-0.4}$	$K_{\mathrm{bknp}} = 43.4^{+3.5}_{-27}$
	2	$E_{\mathrm{p}} = 25.4^{+2.0}_{-4.0}$	$\alpha = 1.2^{+0.3}_{-0.9}$	$\beta = 5.00^{+0.0}_{-2.5}$	$K_{\mathrm{bknp}} = 19.8^{+24}_{-3.3}$
	3	$E_{\mathrm{p}} = 4.9^{+1.3}_{-0.6}$	$\alpha = -2.00^{+3.0}_{-0.0}$	$\beta = 2.9^{+2.1}_{-0.4}$	$K_{\mathrm{bknp}} = 3.69^{+5.2}_{-1.0}$

* T and $K_{\mathrm{bbody}} = R^2_{\mathrm{km}}/D^2_{10}$ are the temperature in units of keV and normalization constant for the black-body radiation model, respectively. R_{km} is the source radius in units of km. D_{10} is the distance to the source in units of 10 kpc. E_{p}, α, β, K_{bknp} are the break energy in units of keV, low energy photon index, high energy photon index, and normalization constant defined in equation (2). K_{bknp} is in units of $\mathrm{keV\,cm^{-2}\,s^{-1}}$.

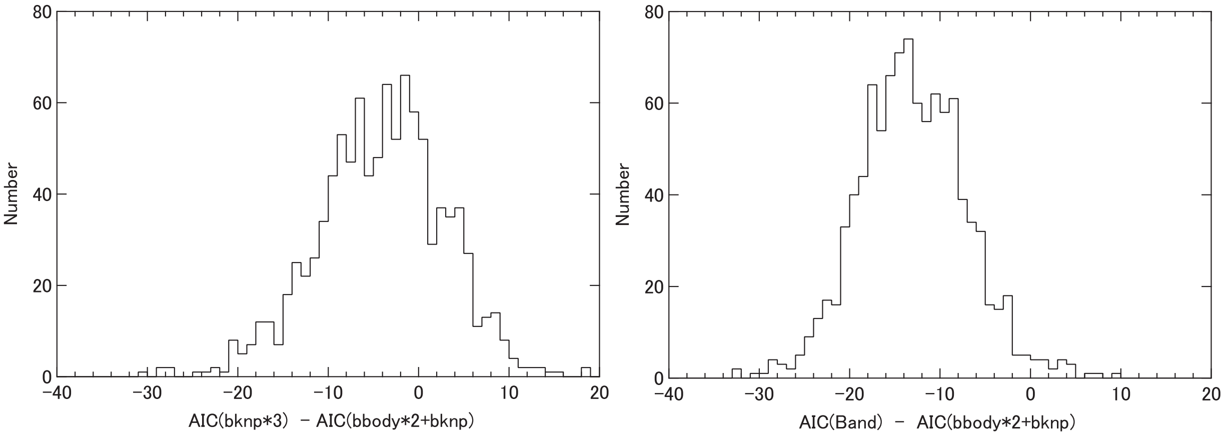

Fig. 4. Left: Simulated distribution of *AIC* differences between the `bknp*3` and `bbody*2+bknp` models. The simulation is performed using the `bknp*3` model, and model fitting to the simulated data is carried out for both the models. The `bbody*2+bknp` model is the most preferable model for the time-integrated spectrum. The *AICs* for the two models were calculated for each simulated spectrum. The fraction of events with $\Delta_{AIC} > 0$ corresponds to the probability of selecting the wrong model. Right: Same plot for the Band model.

Table 5. Isotropic energies $E_{\mathrm{iso},52}$ and rest-frame peak energies $E_{\mathrm{p,src}}$ derived from the average spectrum.

Component	$E_{\mathrm{p,src}}$ (keV)	$E_{\mathrm{iso},52}$
Total*	38.6 ± 2.9	$2.54^{+0.46}_{-0.35}$
A†	$8.4^{+2.2}_{-1.0}$	$0.094^{+0.16}_{-0.08}$
B†	$44^{+3.4}_{-6.9}$	$0.28^{+1.0}_{-0.1}$
C†	123^{+28}_{-17}	$1.36^{+0.4}_{-0.8}$
C'‡	126^{+13}_{-27}	$1.32^{+0.5}_{-0.3}$

* `bknp` model.
† `bknp*3` model.
‡ `bbody*2+bknp` model.

confidence limif (C.L.) In the case of the Band model (right hand panel of figure 4), for 98% of the samples the *AIC* is smaller than the most preferred model `bbody*2+bknp`. The observed *AIC* difference is 13.68, so the Band model is rejected at higher than 98% C.L. All of the three three-component models are acceptable at 90% C.L. The two-component model is rejected at 90% C.L.

Since the time averaged spectrum of GRB 041006 is well represented by a superposition of the three components, we examined the $E_{\mathrm{p,src}}$–E_{iso} relation for each one. The E_{iso} calculated for a model `bknp*3` are summarized in table 5. The E_{iso} calculated for a model `bbody*2+bknp` is also shown in the table for the high-energy component. The result are compared with the other GRBs in figure 3. The components with $E_{\mathrm{p}} > 40\,\mathrm{keV}$ (C) and $E_{\mathrm{p}} \sim 20\,\mathrm{keV}$ (B) are well within the Amati relation, and the component $E_{\mathrm{p}} \sim 6\,\mathrm{keV}$ (A) is out of the 90% distribution width of the Amati relation. The $\log(S_{\mathrm{x}}/S_{\gamma})$ values for the three components are -0.3 for the component C, 0.78 for the component B, and 0.76 for the component A; they are thus classified as XRR, XRF, and XRF, respectively.

3.3. *Time-Resolved Spectral Properties*

A time resolved spectral analysis was performed for 12 independent time intervals, and also for some intermediate intervals that overlap part of one or two adjacent intervals to trace the spectral evolution more closely. We applied multi-component models in the spectral fit, where the model spectrum was represented as a superposition of an arbitrary number of basic functions. The basic functions considered here were black body (`bbody`), broken power law (`bknp`), and a single power law functions (`pl`). The XSPEC built-in model was used for `bbody` and `pl`, for which the XSPEC model names are `bbodyrad` and `powerlaw` respectively. For the broken power law model, we used equation (2).

The fitting results for various combinations of basic functions are summarized in table 6. The fitting parameters for the lowest *AIC* model are given in table 7. The model spectra giving the lowest *AIC* at each interval are shown in figures 5 and 6. The expected number of components constituting the total spectrum is inferred from the number of local excesses in the residual plot for the `bknp` model, and also from the light curves in the four energy bands. As an example, the case of interval 2c is shown in figure 7. The spectrum was fitted with a single broken power-law function, and E_{p} was determined as $\sim 20\,\mathrm{keV}$. Looking at the residual plot shown in the bottom of the figure, local excesses around 6 keV and 60 keV can be seen. Thus, the spectrum of interval 2c is expected to be constituted from three components that have peak energies of 6, 20, and 60 keV. In the case of interval 2b, at least four components are expected from the light curves. One is the precursor component seen in interval 1, which is expected to be present in interval 2 if it is extrapolated smoothly. Two components corresponding to the two peaks seen in the 40–80 keV energy band and one component corresponding to the broad soft emission in the lowest energy band are also expected to be present. Thus, up to four components were examined for interval 2b.

The model selection was carried out by examining the *AIC* difference, and the 90% confidence limit of the *AIC* difference was calculated by performing a Monte Carlo simulation. By this statistical examination, the single-component models considered here were rejected for most of the intervals. The single-component model was accepted only for intervals 1a, 4a, and 4b. For the other intervals, the single-component model

Table 6. Results of a spectral model fitting to the time-resolved spectra.

Interval	Model	n^*	$k^\dagger$	$\chi^{2\ddagger}$	$p^\S$	$AIC^\|$	$\Delta_X{}^\#$	Parameters**
1a	bbody	52	2	41.38	0.802	−7.87	—	$T = 2$
	bknp	52	4	40.75	0.762	−4.68	3.19(3.9)	$E_p = 7.3$
	wabs*pl	52	3	47.26	0.544	1.03	8.90(1.1)	$\alpha = 3.0, n_H = 16$
	pl	52	2	56.57	0.243	8.38	16.25(<0)	$\alpha = 2.1$
1b	bbody*2	52	4	36.27	0.893	-10.73	—	$T = 1.4$,5.9
	bbody+bknp	52	6	35.92	0.857	−7.24	3.49(4.2)	$T = 1.5, E_p = 30$
	bknp*2	52	8	35.60	0.813	−3.70	7.03(7.4)	$E_p = 6$,30
	bknp	52	4	42.92	0.681	−1.98	8.75(<0)	$E_p = 6$
	bbody+pl	52	4	49.93	0.396	5.89	16.62(<0)	$T = 2.1, \alpha = 1.9$
	pl	52	2	63.52	0.095	14.41	25.14(<0)	p = 1.9
2a	bbody*2+bknp	80	8	59.34	0.857	−7.90	—	$T = 1.7$,5.9, $E_p = 84$
	bknp*2	80	8	61.24	0.813	−5.38	2.52(4.1)	$E_p = 24$,83
	bbody+bknp*2	80	10	58.43	0.837	−5.14	2.76(4.2)	$T = 2.6, E_p = 23$,83
	bknp*3	80	12	57.68	0.810	−2.17	5.73(9.4)	$E_p = 5$,24,83
	bknp	80	4	70.48	0.657	−2.13	5.77(0.5)	$E_p = 25$
2b	bbody*2+bknp	80	8	104.91	0.007	37.69	—	$T = 1.4$,5.4, $E_p = 84$
	bbody*2+bknp*2	80	12	99.33	0.008	41.31	3.77(6.2)	$T = 1.4$,5.5, $E_p = 50$,85
	bbody+bknp	80	6	116.18	0.001	41.85	3.99(2.0)	$T = 1.5, E_p = 21$
	bknp	80	4	122.30	0.001	41.96	4.10(1.7)	$E_p = 23$
	bknp*2	80	8	111.59	0.002	42.63	4.77(4.1)	$E_p = 23$,85
	bknp*3	80	12	101.08	0.006	42.71	4.78(8.2)	$E_p = 5$,22,85
	bbody+bknp*2	80	10	106.05	0.004	42.55	5.22(5.5)	$T = 1.5, E_p = 22$,85
2c	bbody*2+bknp*2	73	12	49.53	0.853	−4.32	—	$T = 1.3$,5.0, $E_p = 52$,98
	bbody*2+bknp	73	8	56.66	0.760	−2.50	1.67(<0)	$T = 1.3$,5.0, $E_p = 53$
	bbody+bknp*2	73	10	56.61	0.702	1.44	5.76(0.2)	$T = 1.5, E_p = 18$,54
	bknp*3	73	12	53.58	0.739	1.42	5.74(0.2)	$E_p = 5.5$,18,74
	bknp*2	73	8	62.24	0.574	4.36	8.68(0.06)	$E_p = 19$,54
	bbody+bknp	73	6	66.70	0.488	5.41	9.73(<0)	$T = 4.7, E_p = 55$
	bknp	73	4	87.99	0.006	21.63	25.72(<0)	$E_p = 23$
2d	bbody*2+bknp	66	8	64.70	0.254	14.69	—	$T = 1.2$,4.6, $E_p = 62$
	bbody+bknp	66	6	72.12	0.136	17.85	3.16(0.9)	$T = 4.5, E_p = 62$
	bknp*2	66	8	70.33	0.129	20.19	5.50(1.2)	$E_p = 18$,59
	bknp	66	4	80.21	0.060	20.87	6.18(0.1)	$E_p = 18$
	bbody+bknp*2	66	10	67.50	0.140	21.48	6.79(5.5)	$T = 1.6, E_p = 17$,60
	bknp*3	66	12	66.84	0.113	24.83	10.14(4.4)	$E_p = 4$,17,60
3a	bbody+bknp	74	6	63.37	0.636	0.53	—	$T = 6.8, E_p = 96$
	bknp*2	74	8	63.72	0.557	4.93	4.40(4.9)	$E_p = 27$,95
	bbody+bknp*2	74	10	61.83	0.554	6.71	6.18(6.8)	$T = 6.0, E_p = 50$,92
	bknp	74	4	75.48	0.306	9.46	8.93(3.4)	$E_p = 36$
	bknp*3	74	12	62.21	0.469	11.15	10.62(11.8)	$E_p = 26$,45,96
3b	bknp*2	84	8	80.20	0.349	12.11	—	$E_p = 25$,82
	bknp*2+pl	84	10	79.57	0.308	15.45	3.34(3.9)	$E_p = 26$,84, $\alpha = 1.3$
	bbody+bknp+pl	84	8	83.64	0.257	15.64	3.53(3.0)	$T = 8, E_p = 84, \alpha = 1.6$
	bknp*4	84	16	69.19	0.437	15.69	3.58(8.6)	$E_p = 6$,10,21,84
	bbody+bknp*2	84	10	80.17	0.292	16.08	3.97(4.0)	$T = 0.9, E_p = 26$,80
	bbody+bknp	84	6	85.91	0.413	17.89	5.78(<0)	$T = 8, E_p = 83$
	bknp*3	84	12	79.88	0.245	19.78	7.67(7.2)	$E_p = 5$,26,80
	bknp	84	4	107.35	0.022	28.60	16.49(<0)	$E_p = 67$
3c	bknp*3	73	12	70.36	0.193	21.32	—	$E_p = 26$,44,120
	bbody+bknp*3	73	14	67.43	0.211	22.20	0.88(4.5)	$T = 1.2, E_p = 26$,44,118
	bknp*2	73	8	80.75	0.090	23.37	2.05(2.3)	$E_p = 44$,130
	bbody+bknp*2	73	10	78.07	0.096	24.90	3.58(1.3)	$T = 1.1, E_p = 44$,117

Table 6. (Continued)

Interval	Model	n^*	$k^\dagger$	$\chi^{2\ddagger}$	$p^\S$	$AIC^\|$	$\Delta_X{}^\#$	Parameters**
	bknp*4	73	16	67.91	0.153	26.72	5.40(7.4)	$E_\mathrm{p} = 6{,}26{,}44{,}119$
	bknp	73	4	98.92	0.011	30.18	8.86(<0)	$E_\mathrm{p} = 56$
3d	bbody+bknp	80	6	76.28	0.405	8.19	—	$T = 6.1$, $E_\mathrm{p} = 72$
	bknp*2	80	8	77.40	0.310	13.36	5.17(5.8)	$E_\mathrm{p} = 21{,}47$
	bknp	80	4	86.42	0.194	14.18	5.99(<0)	$E_\mathrm{p} = 24$
	bknp*3	80	12	74.91	0.264	18.74	10.55(13.6)	$E_\mathrm{p} = 23{,}43{,}75$
4a	bbody*2	66	4	59.23	0.576	0.86		$T = 1.2{,}5.2$
	bbody+bknp	66	6	59.14	0.505	4.76	3.90(7.1)	$T = 1.2$, $E_\mathrm{p} = 24$
	bknp	66	4	63.09	0.438	5.02	4.16(2.8)	$E_\mathrm{p} = 26$
	bknp*2	66	8	57.36	0.496	6.74	5.88(7.4)	$E_\mathrm{p} = 4{,}25$
	bbody+pl	66	4	73.06	0.159	14.71	13.85(1.4)	$T = 4.7$, $\alpha = 2.3$
	pl	66	2	100.05	0.003	31.46	30.60(<0)	$\alpha = 2.0$
4b	pl	52	2	47.31	0.582	−0.92	—	$\alpha = 1.9$
	bbody+pl	52	4	44.82	0.604	0.27	1.19(3.1)	$T = 1.5$, $\alpha = 1.8$
	bknp	52	4	45.13	0.591	0.63	1.55(3.6)	$E_\mathrm{p} = 4$
	bbody	52	2	69.71	0.034	19.24	20.16(<0)	$T = 1.7$

* Number of data points used for the fit.
† Number of model parameters.
‡ Chi-square of the fit.
§ Null hypothesis probability.
‖ Akaike information criterion.
\# *AIC* difference between the corresponding model and the lowest *AIC* model. The number in parentheses represents the 90% confidence limit of the *AIC* difference.
** T is the black body temperature in units of keV, E_p is the break energy of the `brknp` model in units of keV, α is the power law photon index of the `pl` model, and n_H is the column density measured in units of 10^{22} atoms cm^{-3}.

considered here was rejected at the 90% C.L. and the multi-component models were preferred.

For most of the intervals, the null hypothesis probability is larger than 0.1. For interval 2b, however, the null hypothesis probability is at most 0.003. This is probably because unknown systematic errors are present in the data.

4. Discussion

The optical afterglow light curve in the R-band could be fitted by a broken power-law model with a break time of $t_\mathrm{b} = 0.16 \pm 0.04$ days (Stanek et al. 2005). Taking t_b as the jet break time and assuming a homogeneous density profile around the GRB, the jet opening angle, θ, was estimated from the following equation (Sari et al. 1999; Nava et al. 2006):

$$\theta = 0.161 \left(\frac{t_\mathrm{b}}{1+z}\right)^{3/8} \left(\frac{n_0 \eta_\gamma}{E_{\mathrm{iso},52}}\right)^{1/8}, \tag{4}$$

where n_0 is the ambient particle density in cm^{-3}, η_γ the radiation efficiency, and $E_{\mathrm{iso},52} = E_\mathrm{iso}/10^{52}$ erg. Assuming $n_0 = 3$ and $\eta_\gamma = 0.2$, we obtained a jet opening angle of $3\overset{\circ}{.}4$. If the GRB is viewed on-axis, the collimation-corrected total energy can be estimated from $E_\gamma = (1 - \cos\theta)\, E_\mathrm{iso}$. The corrected total energies for the three components are $2.4^{+0.70}_{-1.4} \times 10^{49}$ erg for $E_{\mathrm{p,src}} = 123^{+28}_{-17}$ keV (component C), $0.49^{+1.8}_{-0.2} \times 10^{49}$ erg for $E_{\mathrm{p,src}} = 44^{+3.4}_{-6.9}$ keV (component B), and $1.7^{+2.8}_{-1.1} \times 10^{48}$ erg for $E_{\mathrm{p,src}} = 8.4^{+2.2}_{-1.0}$ keV (component A). These values do not follow the Ghirlanda relation (Ghirlanda et al. 2007), except for component A. That is, the $E_{\mathrm{p,src}}$ values expected from the Ghirlanda relation are 39.4, 13.0, and 6.2 keV for the components C, B, and A, respectively. Taking a 5% uncertainty in the Ghirlanda relation, the observed E_p for the components C and B are incompatible.

We also tested the Liang–Zhang relation (Liang & Zhang 2005). The isotropic energies $E_{\mathrm{iso},52}$ calculated by equation (5) of Liang and Zhang (2005) are 2.54, 0.132, 3.28, and 24.1 for components "total", A, B, and C, respectively. The isotropic energy derived from the fit to a single broken power-law function are consistent with the isotropic energy derived from the Liang–Zhang relation. On the other hand, the isotropic energies derived for components B and C are incompatible with those obtained from the relation.

Looking at the time evolution of E_p obtained by the time resolved spectral analysis shown in figure 8, we can identify seven components. Each component is interpolated with a solid line, and is given an identifier: A, $\mathrm{B_1}$, $\mathrm{B_2}$, $\mathrm{C_1}$, $\mathrm{C_2}$, $\mathrm{C_3}$, or $\mathrm{C_4}$.

The most preferred spectral model for component A in interval 1a is the `bbody` model. The calculated emission radius is $4.35^{+1.4}_{-1.1} \times 10^6$ km, which corresponds to 6 solar radii and is a typical radius for a blue supergiant. The *AIC* difference for the second-most preferred `bknp` model is 3.31 and its 90% confidence limit is 4.9, so the `bknp` is also acceptable. The *AIC* differences for the power-law spectrum with and without absorption (`wabs*pl` and `pl`) are larger than 8.9, and their 90% confidence limits are less than 0.3, so these models are rejected at the 90% C.L.

For interval 1b, the acceptable models are `bbody*2`,

Table 7. Fitting parameters for the most preferred models, that is, the model that gives the lowest *AIC*.

Interval	Component	Parameters*			
1a	1	$T = 1.92^{+0.30}_{-0.27}$	$K_{\rm bbody} = 9.94^{+0.71}_{-0.42} \times 10^{1}$		
1b	1	$T = 1.44^{+0.18}_{-0.17}$	$K_{\rm bbody} = 4.17^{+2.2}_{-1.4} \times 10^{2}$		
	2	$T = 5.94^{+1.26}_{-1.08}$	$K_{\rm bbody} = 1.89^{+2.1}_{-0.99}$		
2a	1	$T = 1.60^{+0.84}_{-0.21}$	$K_{\rm bbody} = 2.38^{+7.1}_{-2.3} \times 10^{2}$		
	2	$T = 5.75^{+1.4}_{-1.2}$	$K_{\rm bbody} = 3.95^{+5.9}_{-3.3}$		
	3	$E_{\rm p} = 83.2^{+15.2}_{-10.6}$	$\alpha = 1.45^{+0.20}_{-0.41}$	$\beta = 5.00^{+0.0}_{-1.8}$	$K_{\rm bknp} = 48.9^{+5.8}_{-11}$
2b	1	$T = 1.40^{+0.23}_{-0.17}$	$K_{\rm bbody} = 1.02^{+0.73}_{-0.63} \times 10^{3}$		
	2	$T = 5.40^{+0.59}_{-0.49}$	$K_{\rm bbody} = 13.0^{+6.7}_{-5.7}$		
	3	$E_{\rm p} = 84.3^{+8.4}_{-32}$	$\alpha = 1.26^{+0.46}_{-0.83}$	$\beta = 5.00^{+0.00}_{-0.94}$	$K_{\rm bknp} = 57.8^{+13.9}_{-12.2}$
2c	1	$T = 1.34^{+0.18}_{-0.077}$	$K_{\rm bbody} = 1.44^{+0.56}_{-0.43} \times 10^{3}$		
	2	$T = 5.01^{+1.1}_{-0.46}$	$K_{\rm bbody} = 25.0^{+6.9}_{-13}$		
	3	$E_{\rm p} = 52.3^{+5.0}_{-7.6}$	$\alpha = 0.24^{+1.0}_{-2.2}$	$\beta = 5.00^{+0.0}_{-1.9}$	$K_{\rm bknp} = 97.9^{+35}_{-40}$
	4	$E_{\rm p} = 95.5^{+13.0}_{-9.7}$	$\alpha = 0.06^{+1.4}_{-2.1}$	$\beta = 5.00^{+0.00}_{-1.4}$	$K_{\rm bknp} = 78.4^{+19}_{-50}$
2d	1	$T = 1.28^{+0.47}_{-0.19}$	$K_{\rm bbody} = 1.01^{+0.95}_{-0.85} \times 10^{3}$		
	2	$T = 4.65^{+0.42}_{-0.33}$	$K_{\rm bbody} = 26.3^{+9.7}_{-9.4}$		
	3	$E_{\rm p} = 62.1^{+7.1}_{-11.5}$	$\alpha = 1.22^{+0.3}_{-1.1}$	$\beta = 5.00^{+0.0}_{-1.4}$	$K_{\rm bknp} = 54.1^{+11.5}_{-10.9}$
3a	1	$T = 6.8^{+1.2}_{-1.1}$	$K_{\rm bbody} = 3.61^{+2.9}_{-1.5}$		
	2	$E_{\rm p} = 95.8^{+8.5}_{-15}$	$\alpha = 1.50^{+0.07}_{-0.07}$	$\beta = 5.00^{+0.0}_{-1.5}$	$K_{\rm bknp} = 107^{+17}_{-18}$
3b	1	$E_{\rm p} = 25.3^{+3.5}_{-2.6}$	$\alpha = -0.92^{+1.5}_{-1.1}$	$\beta = 5.00^{+0.0}_{-3.2}$	$K_{\rm bknp} = 68.7^{+11}_{-11}$
	2	$E_{\rm p} = 81.9^{+7.3}_{-9.9}$	$\alpha = 1.05^{+0.15}_{-0.10}$	$\beta = 3.28^{+0.52}_{-0.46}$	$K_{\rm bknp} = 386^{+32}_{-71}$
3c	1	$E_{\rm p} = 25.8^{+2.4}_{-4.0}$	$\alpha = -0.10^{+0.72}_{-1.9}$	$\beta = 5.00^{+0.0}_{-2.8}$	$K_{\rm bknp} = 68.1^{+15}_{-45}$
	2	$E_{\rm p} = 44.0^{+13}_{-3.6}$	$\alpha = -2.00^{+2.7}_{-0.00}$	$\beta = 2.66^{+2.0}_{-0.39}$	$K_{\rm bknp} = 115^{+30}_{-62}$
	3	$E_{\rm p} = 119^{+11}_{-12}$	$\alpha = 1.33^{+0.05}_{-0.11}$	$\beta = 5.00^{+0.00}_{-1.40}$	$K_{\rm bknp} = 159^{+95}_{-48}$
3d	1	$T = 6.05^{+0.71}_{-0.69}$	$K_{\rm bbody} = 5.18^{+2.4}_{-1.6}$		
	2	$E_{\rm p} = 71.9^{+14}_{-30}$	$\alpha = 1.39^{+0.05}_{-0.10}$	$\beta = 4.32^{+0.68}_{-1.5}$	$K = 55.7^{+12}_{-12}$
4a	1	$T = 1.23^{+0.18}_{-0.16}$	$K_{\rm bbody} = 8.09^{+5.6}_{-3.1} \times 10^{2}$		
	2	$T = 5.16^{+0.81}_{-0.71}$	$K_{\rm bbody} = 4.66^{+3.5}_{-2.0}$		
4b	1	$\alpha = 1.93^{+0.16}_{-0.14}$	$K_{\rm pl} = 2.74^{+0.90}_{-0.68}$		

* T and $K_{\rm bbody} = R_{\rm km}^2/D_{10}^2$ are the temperature in units of keV and normalization constant for the black-body radiation model, respectively. $R_{\rm km}$ is the source radius in units of km. D_{10} is the distance to the source in units of 10 kpc. $E_{\rm p}$, α, β, $K_{\rm bknp}$ are the break energy in units of keV, low energy photon index, high energy photon index, and normalization constant defined in equation (2). The unit of $K_{\rm bknp}$ is keV cm^{-2} s^{-1}. $K_{\rm pl}$ is the normalization constant for power law spectrum defined as photon flux at 1 keV in units of photons keV^{-1} cm^{-2} s^{-1}.

`bbody+bknp`, and `bknp*2`, all of which are two-component models. None of the single component models considered here is preferable and all are rejected at the 90% C.L. Thus, it is likely that the emission in interval 1b is composed of two components (A and B_1). The spectral type of each component is not uniquely determined from this result; it is either a black body or a broken power law function. Assuming that component B_1 is black body radiation, the calculated emission radius is about one solar radius.

In intervals 2a–2d, the soft components A and B_1 are present in all the acceptable models. The peak energies of the components are almost constant during intervals 1 and 2, and they decrease slowly, with decay time 72 ± 42 s for component A and 57 ± 33 s for component B_1. Assuming that the components originate from thermal emission, we can derive the evolution of the radiation radii, and they are shown in figure 9 with the filled circles for component A and with open circles for component B_1. The data points for component B_1 are shifted by a factor of four. The data points for intervals 1 and 2 are fitted with a linear function, and we calculate the apparent expansion velocity for component A to be $(6.3 \pm 1.5) \times 10^5$ km s^{-1}, which is twice the speed of light. This superluminal motion is observed when the emitter is moving with relativistic velocity toward the observer. The relation between the

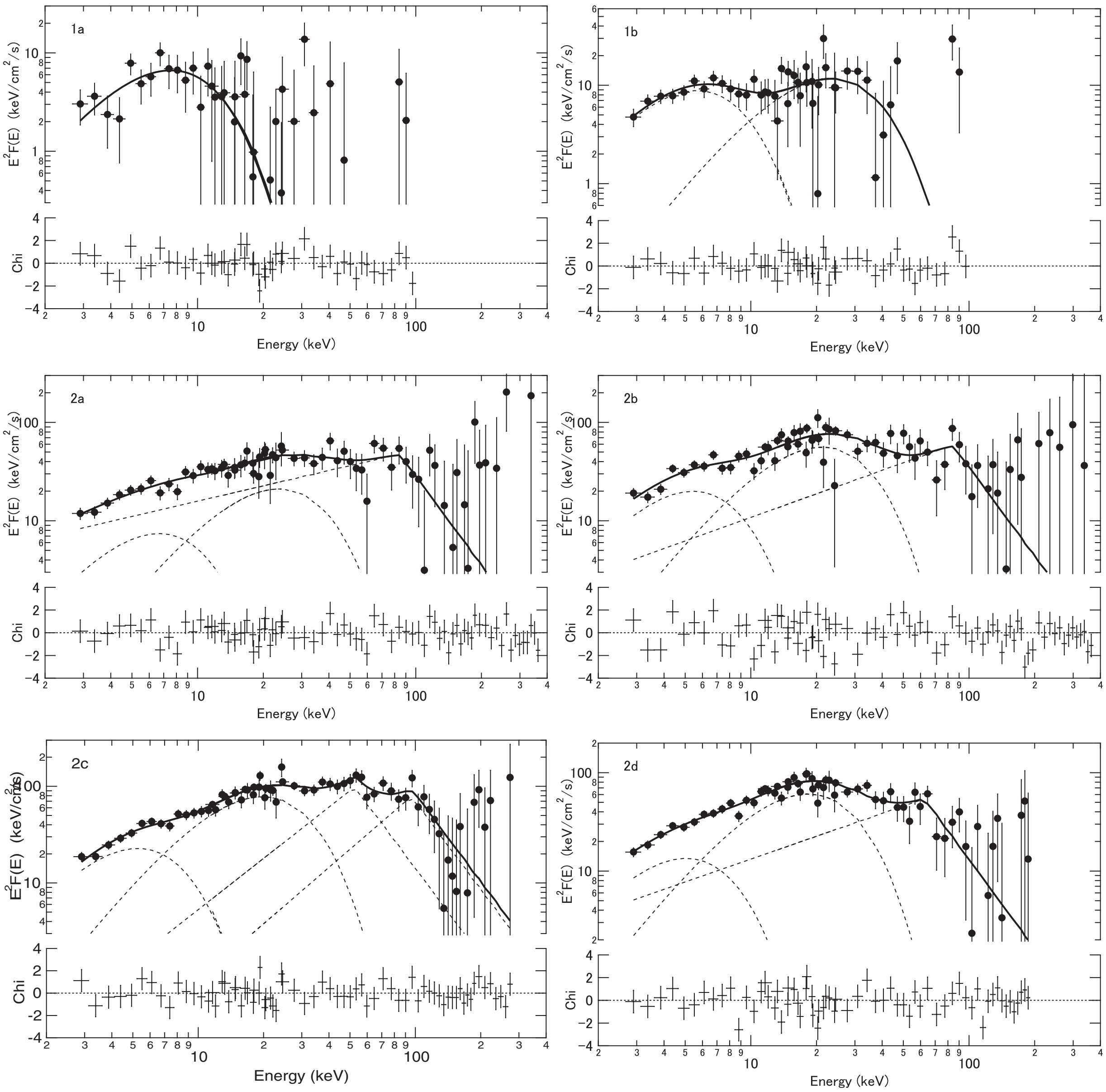

Fig. 5. Time-resolved unfolded spectra for intervals 1 and 2. The residual between the observation and the model is also shown at the bottom panel of each figure. The spectrum is expressed in νf_ν. The most preferable model spectra are plotted as a solid line (total) and dashed lines (basic function).

apparent expansion velocity v and the velocity measured in the source frame v' is given by

$$v = \frac{v'}{(1+z)\left(1-\dfrac{v'}{c}\right)}. \tag{5}$$

The expansion velocity in the source frame is $2.35 \times 10^5\,\mathrm{km\,s^{-1}}$, and the corresponding Lorenz factor is 1.6. The apparent expansion rate for component B_1 is found to be $1.1 \times 10^5\,\mathrm{km\,s^{-1}}$, and the velocity in the source frame is $1.2 \times 10^5\,\mathrm{km\,s^{-1}}$, which is half the velocity of component A. This result indicates that the soft component originates from the GRB photosphere expanding with a mildly relativistic speed. According to the current models of the GRB photosphere (e.g., Meszaros et al. 2002; Rees & Meszaros 2005), however, it is difficult to interpret a blackbody with essentially the same temperature, but an increasing radius, unless the temperature is boosted by the growing Lorentz factor of the photosphere.

If the component originates in an internal shock according to the model of Zhang and Meszaros (2002) the following relation should be satisfied:

$$E_\mathrm{p} \propto L^{1/2}\Gamma^{-2}, \tag{6}$$

where L is the luminosity and Γ is the bulk Lorentz factor of the shock. If the spectral shape does not change, the normalization constant, K, of equation (2) is proportional to the luminosity. As the α and β are not well constrained in the multi-component model due to the correlation of the parameters

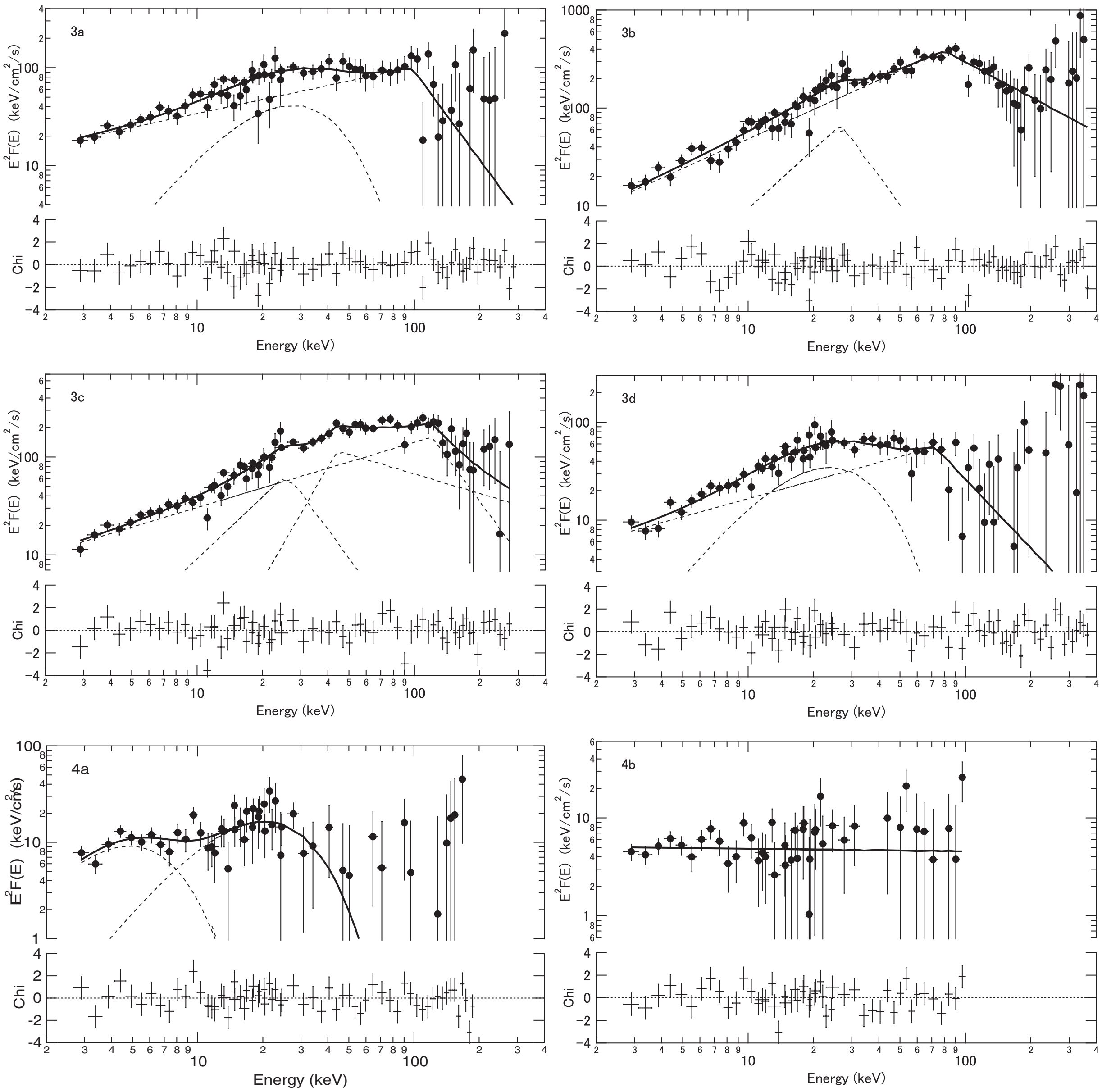

Fig. 6. Time-resolved unfolded spectra for intervals 3 and 4.

among the components, the luminosity is not well constrained. We have plotted the $E_{\rm p}$–K relation in figure 10. If Γ is constant and the spectral shape does not change during the emission, we expect that $E_{\rm p}$ will be proportional to $K^{1/2}$. No clear correlation is found for component A (filled circle). For component B_1 (filled triangle) the expected correlation is not found either, and it shows a negative correlation.

The higher energy components of the interval 2, C_1 and C_2, which correspond to the two peaks seen in the 40–80 keV light curve, are resolved as a broken power law spectrum for which $E_{\rm p}$ is around 50–90 keV. If we assume that $E_{\rm p}$ decreases exponentially, as seen in many GRBs, we can derive the correspondence among the $E_{\rm p}$ as indicated in figure 8. The decay constant of the $E_{\rm p}$ is ~ 20 s.

At interval 3, the first precursor component seen in interval 1a (component A) is not well-resolved. Component B_2 has a similar $E_{\rm p}$ to that of component B_1, but its $E_{\rm p}$ is somehow systematically higher than the extrapolation of B_1. Assuming that B_2 is thermal emission, its radiation radius was calculated, and is shown in figure 9. The radiation radius is well below the extrapolation of those for B_1. The $E_{\rm p}$–K relation of B_2 is shown in figure 10, and it does not follow the relation given by equation (6).

The highly variable spectra, whose emission peaks vary from 100 keV to 40 keV, are also resolved (C_3, C_4), and they correspond to the emissions seen in the light curve of the highest energy band. From figure 8, the $E_{\rm p}$ of the components decrease exponentially with time with a decay constant of ~ 5 seconds.

The $E_{\rm p}$–K relations for components C_1, C_2, C_3, and C_4 are

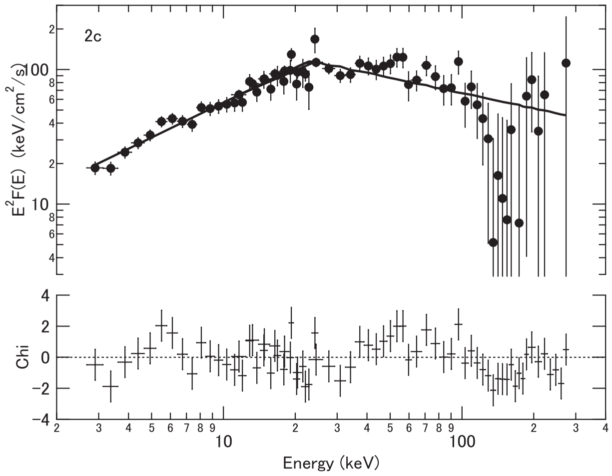

Fig. 7. Example of spectral fitting for interval 2c, where a single-component model was used.

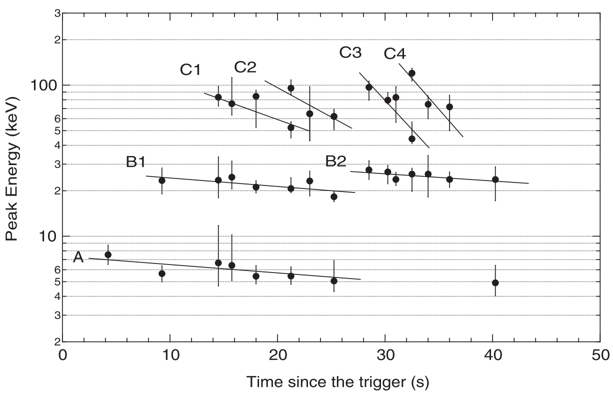

Fig. 8. Peak energy calculated for each interval by fitting the data with multi-component models. The points that are inferred to belong to identical components are interpolated with a line. The vertical error bar corresponds to the 90% confidence limit.

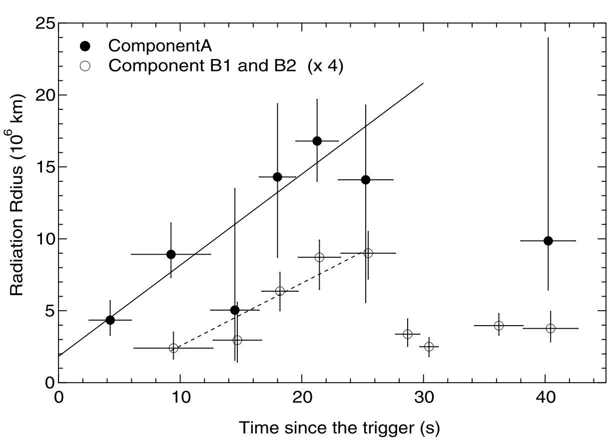

Fig. 9. Evolution of the radiation radii of the blackbody components. The filled circles represent component A of figure 8. The open circles represent components B_1 and B_2, for which the radius is multiplied by four. The solid and dashed lines represent the linear fit to the data of intervals 1 and 2.

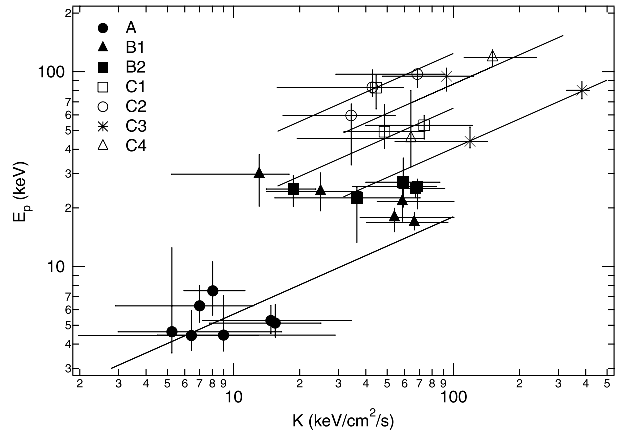

Fig. 10. Relation between E_{p} and K of equation (2) for each component. The solid lines represent the relation $E_{\mathrm{p}} \propto K^{0.5}$.

also shown in figure 10. Although there are few data points for each component, the E_{p}–K relation is satisfied, except for two points. Both the exceptions are at the time intervals corresponding to the rising part of components C_1 and C_3. During the rise, due to the curvature effect, the emission from a part of the shock front that is moving toward us dominates. After that, the emission is averaged over a wider region, so the emission properties may change between the rising part and the following part.

In interval 4a, component B_2 is likely to remain and a black-body spectrum with $T = 1\,\mathrm{keV}$ or a broken power-law spectrum with $E_{\mathrm{p}} \sim 4\,\mathrm{keV}$ is also likely to be present. In interval 4b, a power-law spectrum with photon index of 1.9 is the most preferred model, which is almost the same as the afterglow spectrum observed by Chandra.

5. Conclusion

We analyzed the time-resolved spectra of GRB 041006, and successfully resolved the components corresponding to the hard spikes and the soft broad bump observed in the multi-energy band light curves. The components may be divided into two classes. One is component A, which has almost constant E_{p} around 6 keV, and components B_1 and B_2 which have almost constant E_{p} around 20 keV. E_{p} for this class gradually decreases on a timescale, 60–70 s. The spectral type is well represented by a broken power-law function or a black-body radiation function. Assuming that the emission of this component is due to black-body radiation, we derived the emission radii. At the beginning of the emission they are $4 \times 10^6\,\mathrm{km}$ for component A and $7 \times 10^5\,\mathrm{km}$ for components B_1 and B_2. The expansion velocity in the source frame is also derived; it is $0.78\,c$ and $0.4\,c$ for components A and B_1, respectively. The emission radius of component B_2 is almost constant.

The E_{p}–luminosity relation is examined for these components and compared with the prediction of the internal shock model. We used a normalization constant, K, in equation (2) instead of deriving the luminosity. According to the internal shock model of Zhang and Meszaros (2002), E_{p} is proportional to $L^{1/2}$ if the bulk Lorentz factor of the shock is constant during emission. We could not find such a correlation for components A, B_1, and B_2.

The second class comprises the components whose $E_{\rm p}$ is larger than the former class, and shows a relatively rapid decrease on a timescale of 5–20 s. The spectra are well represented by a broken power-law function, and the $E_{\rm p}$–K relation almost follows the relation expected for an internal shock origin, so this could explain their origin.

We could not reach any conclusion about the origin of the soft component observed for GRB 041006. However, the difference in its time variability with respect to the higher energy component suggests that it originates from different emission sites, such as acceleration by a wider jet, emission from a supernova shock breakout, or emission from the photosphere of the fireball.

We would like to thank the HETE-2 team members for their support. The HETE-2 mission is supported in the US by NASA contract NASW-4690; in Japan in part by Grant-in-Aid 14079102 from the Ministry of Education, Culture, Sports, Science and Technology; and in France by CNES contract 793-01-8479. YS is grateful for support under the JSPS Core-to-Core Program, Grant-in-aid for Information Science (15017289 and 18049074) and Young Scientists (B) (17700085) carried out by the Ministry of Education, Culture, Sports, Science and Technology of Japan. KH is grateful for support under MIT Contract SC-A-293291,

References

Akaike, H. 1974, IEEE Transactions on Automatic Control, 19, 716
Amati, L. 2006, MNRAS, 372, 233
Arnaud, K. A. 1996, in ASP Conf. Ser. 101, Astronomical Data Analysis Software and Systems V, ed. G. H., Jacoby, & J., Barnes, (SanFrancisco: ASP), 17
Atteia, J.-L., et al. 2003, in AIP Conf. Proc. 662, Gamma-Ray Burst and Afterglow Astronomy 2001: A Workshop Celebrating the First Year of the Hete Mission, ed. G. R., Ricker, & R. K., Vanderspek (Melville: AIP), 17
Band, D., et al. 1993, ApJ, 413, 281
Bikmaev, I., et al. 2004, GCN Circ. #2826
Borgonovo, L., Frontera, F., Guidorzi, C., Montanari, E., Vetere, L., & Soffitta, P. 2007, A&A, 465, 765
Butler, N. R., Ricker, G. R., Ford, P. G., Vanderspek, R. K., Marshall, H. L., Jernigan, J. G., Garmire, G. P., & Lamb, D. Q. 2005, ApJ, 629, 908
Cenko, S. B., et al. 2006, ApJ, 652, 490
Da Costa, G., Noel, N., & Price, P. A. 2004, GCN Circ. #2765
Daigne, F., & Mochkovitch, R. 2002, MNRAS, 336, 1271
Fugazza, D., et al. 2004, GCN Circ. #2782
Galassi, M. et al. 2004, GCN Circ. #2770
Garg, A., Stubbs, C., Challis, P., Stanek, K. Z., & Garnavich, P. 2004, GCN Circ. #2829
Ghirlanda, G., Nava, L., Ghisellini, G., & Firmani, C. 2007, A&A, 466, 127
Lazzati, D. 2005, MNRAS, 357, 722
Liang, E., & Zhang, B. 2005, ApJ, 633, 611
Meszaros, P., Ramirez-Ruiz, E., Rees, M. J., & Zhang, B. 2002, ApJ, 578, 812
Murakami, T., Inoue, H., Nishimura, J., van Paradijs, J., Fenimore, E. E., Ulmer, A., & Yoshida, A. 1991, Nature, 350, 592
Nava, L., Ghisellini, G., Ghirlanda, G., Tavecchio, F., & Firmani, C. 2006, A&A, 450, 471
Paczyńsky, B. 1986, ApJ, 308, L43
Page, K. L., et al. 2007, ApJ, 663, 1125
Piro, L., et al. 2005, ApJ, 623, 314
Price, P. A., Roth, K., Rich, J., Schmidt, B. P., Peterson, B. A., Cowie, L., Smith, C., & Rest, A. 2004, GCN Circ. #2791
Ramirez-Ruiz, E., MacFadyen, A. I., & Lazzati, D. 2002, MNRAS, 331, 197
Rees, M. J., & Meszaros, P. 2005, ApJ, 628, 847
Romano, P., et al. 2006, A&A, 456, 917
Sakamoto, T., et al. 2005, ApJ, 629, 311
Sari, R., Piran, T., & Halpern, J. P. 1999, ApJ, 519, L17
Shirasaki, Y., et al. 2003, PASJ, 55, 1033
Soderberg, A. M., et al. 2006, ApJ, 636, 391
Soderberg, A. M., & Frail, D. A. 2004, GCN Circ. #2787
Stanek, K. Z., et al. 2005, ApJ, 626, L5
Umeda, H., Tominaga, N., Maeda, K., & Nomoto, K. 2005, ApJ, 633, L17
Urata, Y., et al. 2007, ApJ, 655, L81
Vanderspek, R., et al. 2004, ApJ, 617, 1251
Vetere, L., Massaro, E., Costa, E., Soffitta, P., & Ventura, G. 2006, A&A, 447, 499
Waxman, E., & Meszaros, P. 2003, ApJ, 584, 390
Zhang, B., & Meszaros, P. 2002, ApJ, 581, 1236